Statistics of Nucleation and Growth of Single Monolayers in Nanowires: Towards a Deterministic Regime

Frank Glas, Federico Panciera, Jean-Christophe Harmand

Statistics of nucleation and propagation of monolayers in nanowires: Towards quasi-deterministic growth

Frank Glas,* Federico Panciera, and Jean-Christophe Harmand

Université Paris-Saclay, CNRS, Centre for Nanoscience and Nanotechnology

10 boulevard Thomas Gobert, 91120 Palaiseau, France

E-mail: frank.glas@c2n.upsaclay.fr

Phone: +33 (0)1 70 27 03 71

Abstract

The vapor-liquid-solid growth of semiconductor nanowires proceeds via the sequential nucleation and extension of atomic or biatomic monolayers at the interface between the solid wire and a liquid catalyst nanodroplet. In the case of III-V compounds, this mother phase contains only a small concentration of the volatile group V atoms. We study experimentally and theoretically the growth regime where there is not enough such atoms available in the liquid at nucleation to complete a whole monolayer. Each monolayer cycle then consists in the rapid formation of a partial monolayer, followed by a slower propagation stage and by a waiting time preceding the next nucleation. We measure the propagation and waiting times of long sequences of monolayers in situ in a transmission electron microscope at three growth temperatures, in a single GaAs nanowire. We model this process and compute the statistics of the characteristic times numerically and analytically. We predict that, at low temperature, the weakness of group V desorption from the liquid should lead to a constant total monolayer formation

time, despite the stochasticity of the nucleation events. The modeling of our experiments yields the values of several crucial growth parameters and provides guidance for the growth of III-V nanowires in a deterministic regime.

Keywords

nanowire, nucleation, vapor-liquid-solid growth, monolayer, statistics, in situ transmission electron microscopy, modeling

The growth of semiconductor nanowires (NWs) in the vapor-liquid-solid (VLS) mode can now be observed in real time at high spatial resolution in dedicated transmission electron microscopes (TEMs). Such *in situ* experiments confirm many of the basic tenets of recent theories of NW growth.[1–9] In particular, the NWs usually grow monolayer (ML) by ML,[5,10–14] each ML starting *via* a single nucleation event occurring at the interface between the solid NW and the apical liquid nanodroplet.[12]

In the case of NWs of III-V compounds, whatever the catalyst, the volatile group V element is present at very low concentration (on the order of 1%) in the liquid droplet.[7,15] The formation of even a single ML may then significantly deplete the droplet of this element, which has a strong impact on the timing of the nucleation events and thus on their statistics.

Indeed, we previously observed (*ex situ*, *i.e.* after growth) that the numbers of MLs formed during successive equal times have a sub-Poissonian distribution,[16] contrary to what would result from independent nucleation events. We interpreted this in terms of an anticorrelation in time of the nucleation events: because of droplet depletion, the chemical potential of a III-V pair in the droplet, and thus the nucleation probability, are less after a first nucleation event than just before. We modeled this *nucleation antibunching* numerically[16] and analytically.[17] We also showed that it may produce very uniform length distributions in NW ensembles,[18] such as were later observed.[19,20] This analysis assumed that the time for ML completion (after nucleation) is very short compared with the interval between successive

nucleations. This requires in particular that enough group V atoms are available in the liquid at nucleation to complete rapidly the solid ML (Figure 1a). In addition, *in situ* experiments and calculations show that, at large droplet contact angles, the solid-liquid interface may be non planar: along at least part of the triple phase line (TPL) bordering the NW top facet, a solid wedge is missing and occupied by liquid.[5,10,11,14,21] The volume of this "truncation" varies in phase with the ML formation cycles. In particular, it increases abruptly when a new ML nucleates. The atoms thus removed from the already formed NW feed the growing ML and allow it to form in a very short time[11] even when there are not enough atoms in the droplet at nucleation. These two cases are not considered in the present work.

Instead, we study experimentally and model a regime where the number of group V atoms available at nucleation is even less than the group V content of a ML and where the missing atoms cannot be provided by solid truncation. *In situ* investigations suggest that this could happen frequently.[11–14] We shall see that the kinetics and statistics of nucleation are then deeply modified, which produces another type of antibunching.

In a previous *in situ* investigation, we observed in real time the formation of successive MLs of GaAs NWs grown by molecular beam epitaxy (MBE) in the Au-catalyzed VLS mode.[12] We focused on the regime of interest here, with a flat solid-liquid interface, which prevails at intermediate contact angles and usually produces the wurtzite (WZ) crystal phase.[11,14] By tilting this interface with respect to the electron beam (as in Figure 1d), we could observe three stages in the formation of each ML (Figure 1c,e): the coverage θ of the interface by the new ML first increases abruptly (stage 1) and then much more slowly and quasi-linearly (stage 2). Once the ML is complete, no further growth occurs for a finite amount of time (stage 3), before the next ML starts forming, a clear sign of the mononuclear character of the process.[12] We interpreted our observations as follows (Figure 1b,c). Stage 1 comprises nucleation, itself too elusive to be observed (the critical nucleus probably consists of only a few III-V pairs[7,22]), and fast initial expansion of the ML using the As atoms available in the liquid. We argued that, in case of shortage of As atoms, this expansion ends

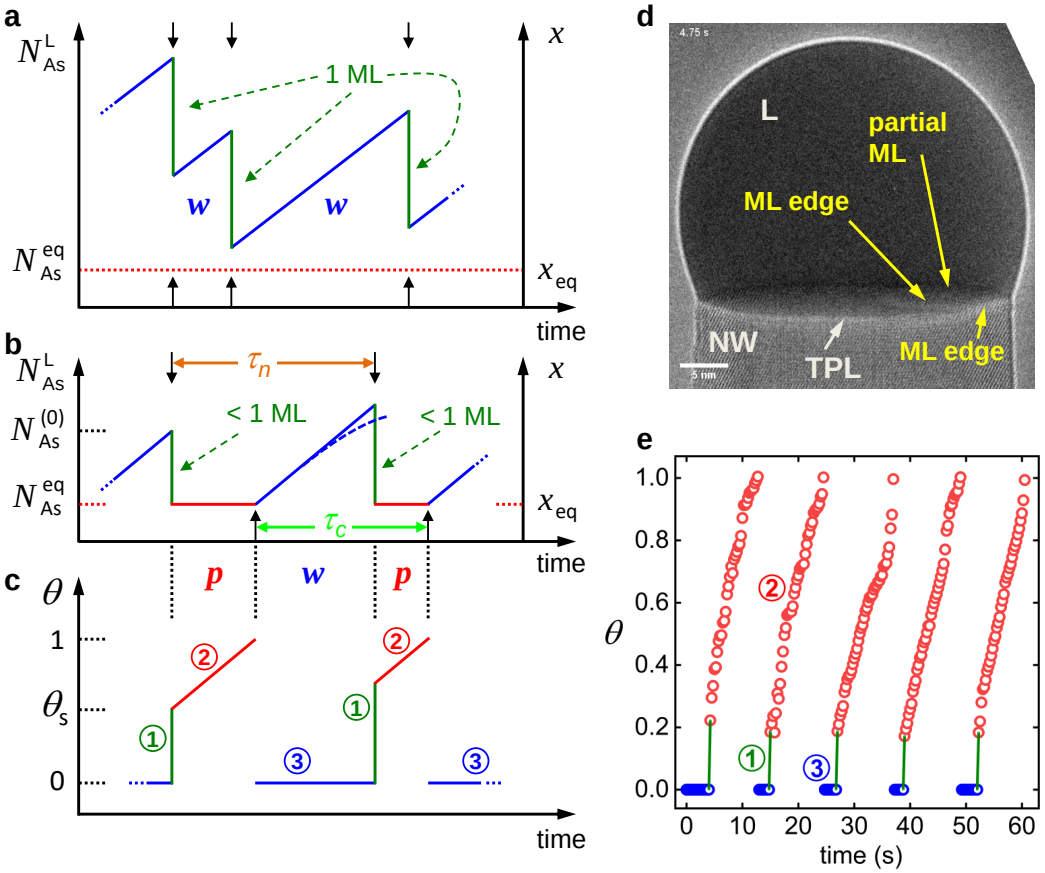

Figure 1: (a,b) Schematics of the time variations of the numbers of group V atoms (left axis) and corresponding atomic concentration (right axis) in the liquid catalyst droplet, in the two growth regimes. Down and up arrows mark the nucleation and completion of the MLs, respectively, and red dotted lines the liquid/solid equilibrium values. (a) Previously studied antibunching regime, with enough group V atoms in the droplet to complete the ML very rapidly after nucleation.[16,17] (b) The regime studied here, where the atoms available at nucleation correspond only to a fractional ML. (c) Schematics of the fractional ML coverage θ corresponding to (b), with the three stages of the ML cycle indicated. Propagation time p covers the extension of the fractional ML and waiting time w the interval between ML completion and next nucleation, during which, due to desorption, x may increase sublinearly (dashed curved in (b)). $N^{(0)}_{As}$ and θ_s (here indicated for the first ML) vary between MLs. (d) TEM image (from Movie1) of a ML propagating at the interface between a GaAs NW and a (Ga,As) droplet (L). (e) Variation with time of the interface coverage by five successive MLs, with the three stages indicated (from Movie1).

at the equilibrium "stopping size" (coverage θ_s) introduced by Dubrovskii in the field of NW growth[23] (see point (a) below). Extension during stage 2 is slower since it depends on the external As beam refilling the droplet. Stage 3 is a waiting time during which, upon further refill, As concentration and chemical potential build up in the droplet until they become sufficient to induce a new nucleation.

This scenario is likely but cannot be confirmed experimentally, since the As content of the liquid is too low to be measured. However, our interpretation is supported by a recent theoretical study by Glas and Dubrovskii of the formation of a single ML, that relates quantitatively, throughout the ML cycle, the ML geometry to the As content of the liquid.[24] In this work, we developed a simple kinetic model that describes analytically a whole range of ML growth regimes as a function of the competition between transfer and attachment of atoms to the growing ML on the one hand and refill of the droplet by the external fluxes on the other. The regime with a short stage 1 and a long stage 2 is obtained when transfer and attachment are fast. In this case, the formation of the ML may be treated as a quasistatic process and we could determine, as a function of the group V content of the droplet at nucleation, (i) the ML fraction that forms at stage 1 and, in case this fraction is less than 1, (ii) the partition of the new atoms provided at stage 2 between incomplete ML and liquid, and thus the extension rate of the ML. The main results, illustrated by the matching panels b and c of Figure 1, yield the following rules:

(a) An incomplete ML forms at stage 1 if, due to transfer to this ML, the depleted liquid reaches equilibrium with it. This is an instance of a general phenomenon affecting nucleation and growth from small size mother phases, which has been much studied theoretically[25–28] and invoked previously in the case of vapor-solid-solid NW growth.[29] In principle, the equilibrium concentration depends on the energy of the ML edge. Of course, because of refill, this equilibrium is only transitory.

(b) For self-catalyzed GaAs NWs, if the specific ML edge energy is low, then, at the end of stage 1, the droplet As content gets very close to the value corresponding to equilibrium

between liquid and *bulk* solid and remains nearly fixed to this value during stage 2. This means that all new atoms provided by the vapor only transit *via* the liquid to the ML.[24]

RESULTS AND DISCUSSION

Experiments. Further *in situ* MBE growth experiments were carried out on self-catalyzed WZ GaAs NWs in the NanoMAX microscope used in our previous work,[12] as described in Section Methods and illustrated by Movie1. They reveal the same three stages as our prior experiments (Figure 1d,e), but this time, we measured the durations of these stages over long sequences of MLs in a single NW, at different temperatures. Stage 1 is too fast to be resolved and is considered to be instantaneous. The durations of stages 2 and 3 are ML propagation time p and waiting time w, respectively (Figure 1b,c,e). We also measured the duration of successive ML cycles as the intervals between either nucleation events (τ_n) or ML completions (τ_c). Nucleation being a stochastic phenomenon, any of these characteristic times τ varies between MLs. Its average $\bar{\tau}$, and more generally the statistical properties of its distribution (standard deviation σ_τ in particular), are however well defined (at least for a given NW), since care was taken to maintain constant growth conditions in terms of MBE fluxes and substrate temperature. Figure 2 shows the variations with nominal growth temperature $T^{(n)}$ of $\bar{\tau}$ and σ_τ for $\tau = w$, p, τ_c and τ_n in a single NW.

Purpose of modeling. In the nucleation antibunching regime investigated previously,[16,17] the group V concentration in the liquid varies relatively little around an average; the liquid droplet is never depleted enough to reach equilibrium with the solid and a full ML can form quickly after nucleation (Figure 1a). The new regime described above and sketched in Figure 1b,c differs in all these respects. However, it clearly produces another type of antibunching: with the liquid at equilibrium, the nucleation probability remains zero throughout propagation time and is very small at the beginning of waiting time. In addition, interesting correlations appear: the longer the waiting time, the larger the number $N_{\mathrm{As}}^{(0)}$ of

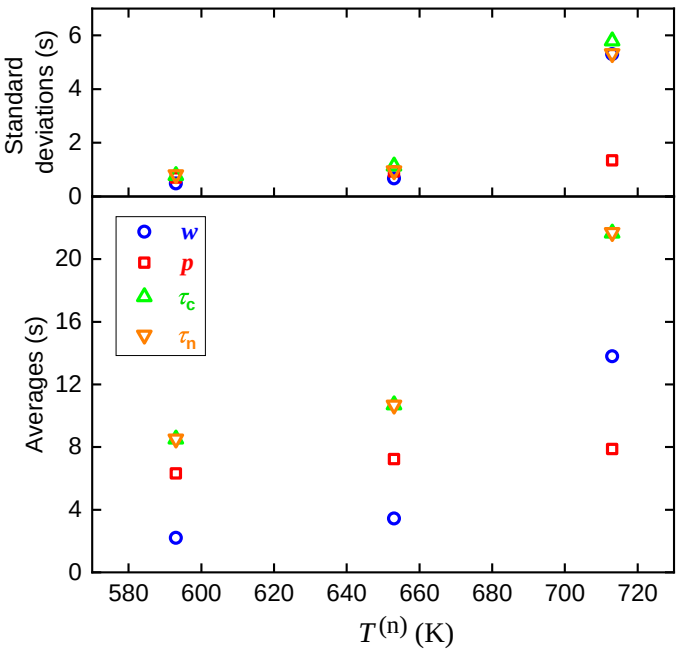

Figure 2: Variation with nominal growth temperature of the averages and standard deviations of the four characteristic times. Data were acquired on a single NW which was maintained at each temperature long enough to produce extended sequences of MLs (about 200 at $T_l^{(n)} = 593$ K and $T_m^{(n)} = 653$ K, and 60 at $T_h^{(n)} = 713$ K).

As atoms in the liquid at nucleation (Figure 1b) and the fractional ML formed (Figure 1c), and therefore the shorter the following propagation time. This will regulate the duration of the ML cycle.

Our aim is to explore this new regime by combining growth modeling and experiments. We will attach particular importance to the statistics of the various characteristic times, to the effects of temperature, and to extracting meaningful physical parameters. We previously developed a comprehensive model of the self-catalyzed MBE growth of GaAs NWs of zinc blende (ZB) structure, from which we derived values of the two parameters governing the corresponding nucleation rate (see eq 2 below).[7] This model included neither interface truncation (often observed in ZB NWs[14]) nor liquid depletion (As concentration and nucleation probability were taken as constant), nor statistical fluctuations. This could be a good approximation for NWs of relatively large radius, but we are here interested in the opposite situation, with a large cyclic depletion and significant statistical fluctuations. Moreover,

due to the difference of structure and hence of nucleation *locus*,[4,12,30] there is no guarantee that the nucleation rate parameters obtained in our previous study[7] can be transferred to the WZ structure. One aim will thus be to find such parameters. We also want to explore theoretically a wider range of growth conditions than so far investigated experimentally, in order to find out situations that minimize the statistical fluctuations of the duration of the ML cycles, which hinder the deterministic fabrication of NWs and the assembly of uniform ensembles thereof.[18]

Model. The following model and calculations would apply to any III-V NW growing in conditions such that the amount of group V atoms in the droplet is insufficient to produce a full ML at stage 1. However, to simplify the discussion and to make quantitative comparison with our experiments, we consider self-catalyzed GaAs NWs. In this case, the catalyst droplet consists nearly entirely in the group III (Ga) element with a small amount of group V (As) atoms,[7] and ML extension can only be hindered by a shortage of the latter. At given temperature T, the state of the binary liquid is set by the atomic concentration x of As. The numbers of Ga and As atoms removed from the liquid to form any amount of the solid NW are equal, and we consider constant and equal rates of refilling of the droplet for Ga and As (by the direct and re-emitted beams[7,31–33] and by surface diffusion,[34] which might even operate for group V species[33]). We assume a constant NW radius and neglect the small variations of droplet contact angle induced by depletion and refilling.[24] If N_i^L is the number of atoms of species i in the liquid, $N_{\rm As}^L << N_{\rm Ga}^L$ at any time and the relative variations of $N_{\rm Ga}^L$ are minute. Hence, $x << 1$ and, for a given NW, $x \cong N_{\rm As}^L/N_{\rm Ga}^L$ with a fixed $N_{\rm Ga}^L$.

In the present experiments, we never observe the rapid formation of a full ML after nucleation (p never cancels). We thus focus our theoretical study on conditions where there is *never* enough As atoms present in the liquid at nucleation to build a complete ML. Of course, this should not be the case for broad NWs,[24] an extreme instance being schematized in Figure 1a, with *always* enough As at nucleation to build a ML. Intermediate cases also likely exist where, due to fluctuations, there is enough As to build a full ML at the nucleation

of certain MLs and not enough for others. This regime will be studied elsewhere.

We thus assume that the variation of the As content of the droplet during the growth of each ML obeys rules (a) and (b) given above, with $p \neq 0$. The formation of a few successive MLs is sketched in Figure 1b,c. At nucleation (down pointing arrow, green lines), a fractional ML forms using all As atoms available, namely $N_{\mathrm{As}}^{(0)} - N_{\mathrm{As}}^{eq} < N_{\mathrm{ML}}$, with N_{As}^{eq} the number at bulk liquid-solid equilibrium and N_{ML} the total number of pairs in a ML. Note that $N_{\mathrm{As}}^{(0)}$ and thus the fractional coverage θ_s vary between MLs. During stage 2, no incoming As atom serves to enrich the liquid. It is thus either incorporated to the ML or desorbs, and x remains equal to x_{eq} (red lines). After ML completion, x increases again until next nucleation (blue lines).

Our calculations, carried out in the framework of classical nucleation theory (CNT), rely on an expression of the probability of nucleation per unit time, P_n, as a function of x. To account for the nucleation *locus*, we write[7,30]

$$P_n = \Sigma_n \; J_n \tag{1}$$

with Σ_n the area available for nucleation and J_n the nucleation rate, which we express as:[7,35]

$$J_n = A \; x \left(\frac{\Delta\mu}{k_B T}\right)^{1/2} \exp\left(-\frac{\Delta G_c}{k_B T}\right) \tag{2}$$

In eq 2, prefactor A is independent of x but may depend on temperature, $\Delta\mu$ is the difference of chemical potential per III-V pair between the liquid of composition x and the binary solid (see Supporting Information S1), ΔG_c is the nucleation barrier and k_B Boltzmann's constant. As usual in CNT, we consider nuclei of fixed shape with linear size r, perimeter $\alpha_1 r$ and area $\alpha_2 r^2$ (with α_1, α_2 shape-dependent constants). If γ_e is the average effective surface energy of the vertical edge of the 2D nucleus,[4,7] the size of the critical nucleus and the nucleation barrier are $r_c = b/\Delta\mu$, $\Delta G_c = B/\Delta\mu$, respectively, with $b = \alpha_1 a^3 \gamma_e / (8\alpha_2)$, $B = \alpha_1^2 a^4 \gamma_e^2 / \left(16\sqrt{3}\ \alpha_2\right)$. Strictly speaking, this holds for ZB NWs growing along the $< 111 >$ axis, with a the lattice

parameter, but this can safely be used for our $< 0001 >$-oriented WZ NWs.

The location of the 2D nucleus at the solid-liquid interface is of the utmost importance for NW growth, in particular as regards polytypism.[4] We assume the interface to be bounded by a hexagonal TPL of radius (center-corner distance) R and area $S_H = 3\sqrt{3}R^2/2$. Nucleation may occur equiprobably over the whole interface (then $\Sigma_n = S_H$) or only in a narrow band along the TPL, which width scales with the critical radius.[4,30] However, our *in situ* study of the formation of WZ GaAs MLs revealed that, at the end of stage 1, the fractional ML is a rhomboid systematically located at a TPL corner (as in Figure 1d) and we showed that this makes extremely likely that nucleation occurs there as well.[12] In this special case of nucleation at the TPL, the area available for nucleation at each corner simply equals the critical nucleus area. With rhomboidal nuclei of side r_c ($\alpha_2 = \sqrt{3}/2$) and nucleation equiprobable at the six corners, then $\Sigma_n = 3\sqrt{3}r_c^2$ (if $r_c < R/2$).

Numerical simulations and first discussion. We simulated the growth of single NWs as previously described.[16,18] The growth sequence is divided in short elementary time steps. At each step, the nucleation probability P_n is calculated using eqs 1 and 2 for the current liquid composition x and the occurrence of a nucleation event during the time step is drawn accordingly. If nucleation occurs, x is updated to x_{eq} and a fractional ML containing $(x - x_{eq})\, N_{\mathrm{Ga}}^{L}$ pairs is formed; if not, x is increased according to constant external input minus desorption.[7] x is initially set to a reasonable value, but the system very quickly looses memory of this initial condition, and the first ML cycles are ignored.

Figure 3a-c shows extracts of such simulations for a NW of radius $R = 7$ nm submitted to a given incident As flux, which illustrate the dramatic changes with growth temperature of the patterns of As concentration and characteristic times. We keep in mind that desorption rate and equilibrium concentration increase with temperature and that, at given T, As desorption also increases with x.[7] Hence, on average, all characteristic times increase with temperature. However, p increases more slowly than w since x remains at its lowest during propagation time whereas it increases during waiting time (Figure 1b). At the lowest

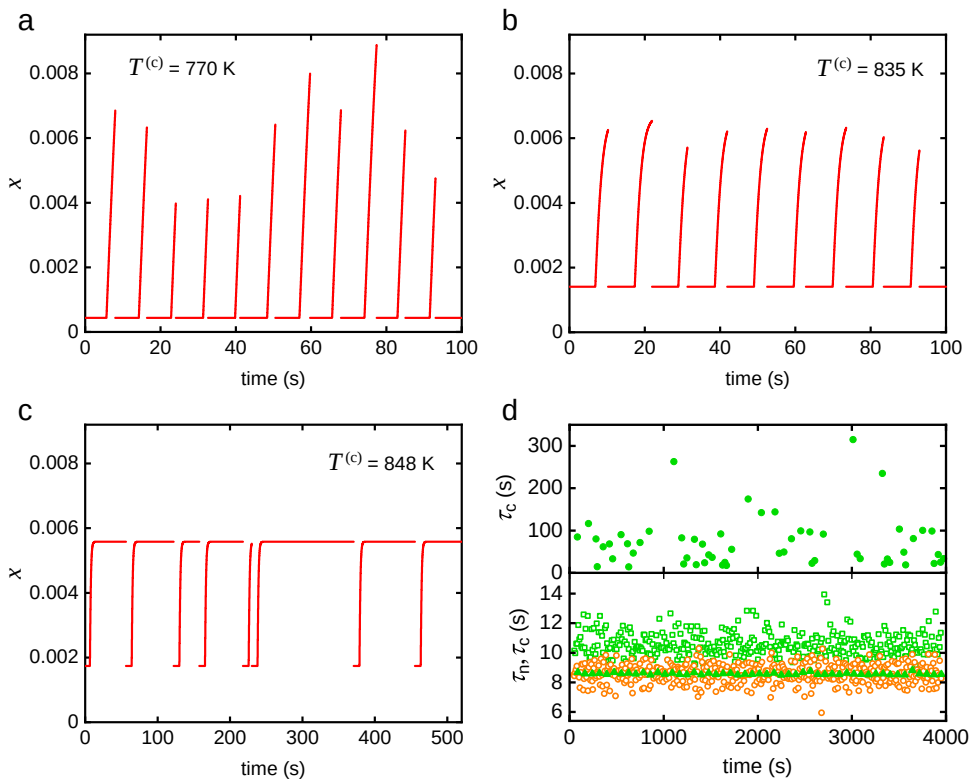

Figure 3: Extracts of simulations (with time step 0.8 ms) of the growth of a GaAs NW at different temperatures $T^{(c)}$. The NW, of radius $R = 7$ nm, with a droplet contact angle $\beta = 100°$, is submitted to an effective As flux producing a growth rate of 0.118 ML s^{-1} in absence of desorption from the liquid. (a,b,c) Variation of the As concentration in the liquid droplet at $T^{(c)} = 770,\ 835$ and 848 K. (d) Characteristic times τ_n between successive nucleations at $T^{(c)} = 770$ K (orange circles), and τ_c between ML completions at $T^{(c)} = 770$ K (green triangles, with every tenth value plotted, to avoid overlap), 835 K (green open squares) and 848 K (green disks, upper panel).

temperature (Figure 3a), As desorption remaining negligible, x increases linearly during the waiting time (as sketched in Figure 1b). Hence, the droplet content at the nucleation ending waiting time w is $N_{\rm As}^{(0)} = N_{\rm As}^{eq} + \rho w$ with ρ the constant rate of input of As atoms into the droplet. The fractional ML built at nucleation contains $N_f = N_{\rm As}^{(0)} - N_{\rm As}^{eq} = \rho w$ As atoms. Since desorption is even less during ML extension, the *following* propagation time p verifies $\rho p = N_{\rm ML} - N_f$. Hence, $\tau_c = w + p = \rho^{-1} N_{\rm ML}$, as indeed expected in absence of desorption. Accordingly, our simulations show a nearly constant τ_c (green triangles in Figure 3d). This remarkable uniformity contrasts with the broad distributions of the waiting time (related to

a wide range of As content at nucleation) and of the interval τ_n between nucleations (orange circles in Figure 3d), which is the sum of the waiting time and the *preceding* propagation time (Figure 1b). The reset of the As content to its equilibrium value during ML propagation (stage 2) eliminates any correlation with the past, so that the following nucleation event, and thus w, are not affected in any way by the preceding propagation time.

As temperature increases (Figure 3b), desorption starts manifesting itself *via* a sub-linear increase of x during waiting time, particularly noticeable at the highest As concentrations explored before nucleation. Hence, $N_{\mathrm{As}}^{(0)}$ still depends directly on w, albeit non-linearly. The following propagation time p is set by N_f (and the fixed desorption rate at x_{eq}) and thus by $N_{\mathrm{As}}^{(0)}$. However, remarkably, even moderate desorption and the ensuing non-linearity can severely reduce the anticorrelation between w and following p, which means that τ_c (green open squares in Figure 3d) is now also broadly distributed.

Desorption then increases very rapidly with temperature. A modest rise of 13 K (Figure 3c) alters the pattern considerably. For most MLs, due to strong desorption from the liquid, the stage 2 As concentration quickly becomes very close to the stationary value $x_s(T)$ at which desorption balances incorporation. If x_s is low enough for the nucleation rate to be small, the system may remain on this plateau for extended periods, which moreover become very broadly distributed, and so does w. On the contrary, we expect the propagation time p to become narrowly distributed: since most nucleations occur at $N_{\mathrm{As}}^{(0)}$ nearly fixed to $x_s N_{\mathrm{Ga}}^{L}$, N_f is also fixed. In turn, this sets p since, here again, it only depends on N_f and on the known desorption rate at the elevated x_{eq}.[24] Any anticorrelation is now effectively lost. With p and w narrowly and broadly distributed, respectively, τ_c becomes very broadly distributed (green disks in Figure 3d).

The predicted plateauing of x at high temperature is akin to the so-called *incomplete condensation* occurring in crystal growth from a vapor.[36,37] This phenomenon has already been invoked in its standard form to account for the very long incubation times observed in the *catalyst-free* growth of GaN NWs, *via* the rapid desorption of adatoms from dielectric or

metallic substrates.[38] The present variant is specific to VLS growth, with nucleation hindered by the high desorption rate of As from the liquid. Moreover, it operates throughout growth, whereas, for GaN NWs at least, the sticking coefficient of the volatile species becomes much larger once some NWs have nucleated.[38,39]

Most of these trends feature in our experiments (Figure 2). For instance, $\bar{w}$ and $\bar{p}$ both increase with T, but the latter much less than the former. As predicted (Figure 3d), the standard deviation of τ_c increases sharply with T. Experiments also confirm that $\sigma_p << \sigma_w$ at high temperature, although not to the point of tending to 0, and we do not observe the very narrowly distributed τ_c predicted at low temperature. Before discussing these findings in detail, we show that, in absence of desorption, the statistical properties of the distributions of the various characteristic times can be calculated analytically.

Analytical calculations. The distributions of propagation times p and waiting times w can be calculated analytically, under the hypotheses used in the simulations and in the limit of negligible As desorption from the droplet. We introduce the reduced As concentration (thereafter 'concentration') in the liquid, $\tilde{x} = x/x_{eq}$ ($\tilde{x} = 1$ at equilibrium) and $\tilde{x}_{\mathrm{ML}} = N_{\mathrm{ML}}/N_{\mathrm{As}}^{eq}$. The As atoms provided to the system in time interval δt increase $\tilde{x}$ by $\tilde{\rho}\,\delta t$, with $\tilde{\rho} = \rho/\left(N_{\mathrm{Ga}}^{L} N_{\mathrm{As}}^{eq}\right)$. According to rule (b), these atoms either contribute to ML extension (stage 2) or remain in the droplet (stage 3).

Let us assume that nucleation occurs at time $t = 0$, when concentration is $\tilde{x}_0$, with $1 \leq \tilde{x}_0 < \tilde{x}_{\mathrm{ML}} + 1$ (rule (a)). According to our model, $\tilde{x}$ instantaneously reduces to 1 and remains fixed to this value during time p. In absence of desorption and with all incoming atoms incorporating to the new ML (rule (b)), the propagation time is:

$$p = \frac{1}{\tilde{\rho}}\left(1 + \tilde{x}_{\mathrm{ML}} - \tilde{x}_0\right) \tag{3}$$

After ML completion and before the next nucleation, $\tilde{x}$ increases with time as $\tilde{x}(t) = 1 + \tilde{\rho}t$ and the nucleation probability as $P(t) = P_n\left[\tilde{x}(t)\right]$, with P_n given by eqs 1 and 2. Thus,

the probability per unit time for the next nucleation to occur after waiting time w, *i.e.* the density of probability of the waiting time, is:[17]

$$\begin{aligned} \pi_w(w) &= P(w) \exp\left\{ -\int_0^w P(t)dt \right\} \\ &= P(w) \exp\left\{ -\frac{1}{\tilde{\rho}} \int_1^{1+\tilde{\rho}w} P_n(\tilde{x})\ d\tilde{x} \right\} \end{aligned} \tag{4}$$

To proceed, we need an analytical expression of the nucleation rate J_n, and hence of the difference of chemical potential $\Delta\mu$. For III-V compounds, at a given temperature T, $\Delta\mu$ is very well approximated by expression

$$\widehat{\Delta\mu}\,(x,T) = \alpha_\mu\ k_B T \ln(\tilde{x}) \tag{5}$$

with α_μ a temperature-dependent constant on the order of 1. The equilibrium concentration, which features in the definition of $\tilde{x}$, also depends on temperature (and on group III concentration in the liquid for metal-catalyzed growth[15]) and on the crystal phase. Supporting Information S1 shows that this approximation is excellent for self-catalyzed GaAs and gives some values of parameters α_μ and x_{eq}.

From eqs 1 and 2 and the expressions of Σ_n (for nucleation at corners) and $\Delta\mu$, we get:

$$\int_1^{1+\tilde{\rho}w} P_n(\tilde{x})\ d\tilde{x} = A_c\ U_c\,(1+\tilde{\rho}w) \tag{6}$$

with

$$A_c = \alpha_\mu^{-3/2} \alpha_c \alpha_2 A x_{eq} b^2 (k_B T)^{-2} \tag{7}$$

$$U_c\,(X) = \int_1^X u\,(\ln u)^{-3/2} \exp\left(-\frac{B_T}{\ln u}\right) du \tag{8}$$

$$B_T = \alpha_\mu^{-1} B (k_B T)^{-2} \tag{9}$$

$U_c(X)$ rewrites as:

$$U_c(X) = 2\int_{(\ln X)^{-1/2}}^{+\infty} \exp\left(\frac{2}{v^2} - B_T v^2\right) dv \tag{10}$$

Using results 7.1.2, 7.1.3, 7.1.10, 7.1.11 and 7.4.34 in Ref. 40, we find:

$$U_c(X) = -\sqrt{\pi}\ B_T^{-1/2} \left[F_c(v)\right]_{(\ln X)^{-1/2}}^{+\infty} \tag{11}$$

with

$$F_c(v) = \Re\left\{\phi(v)\right\} \tag{12}$$

$$\phi(v) = \exp\left(2\sqrt{2}B_T^{1/2}\ i\right)\ \mathrm{erfc}\left(B_T^{1/2}v + i\frac{\sqrt{2}}{v}\right) \tag{13}$$

Here, $\Re$ denotes the real part of a complex number, i the imaginary unit and erfc the complex complementary error function.[40] Since the erfc term tends to 0 when $v \to +\infty$,[40] we find:

$$U_c(X) = \sqrt{\pi}\ B_T^{-1/2} F_c\left(\left[\ln X\right]^{-1/2}\right) \tag{14}$$

and, finally, from eqs 4 and 6:

$$\pi_w(w) = P_n(1+\tilde{\rho}w)\ \exp\left[-\frac{A_c}{\tilde{\rho}}\ U_c(1+\tilde{\rho}w)\right] \tag{15}$$

As noted above, in the absence of desorption, $\tau_c = w + p$ is fixed, provided p is the propagation time *following* waiting time w. The density of probability of the propagation time is thus simply:

$$\pi_p(p) = \pi_w\left(\tau_c - w\right) \tag{16}$$

On the other hand, waiting time w is independent of the *preceding* propagation time p.

The density of probability of their sum τ_n (the interval between nucleations) is thus:

$$\begin{aligned} \pi_{\tau_n}(\tau_n) &= \int_{w_m}^{\tau_n} \pi_w(w)\ \pi_p(\tau_n - w)dw \\ &= \int_{w_m}^{\tau_n} \pi_w(w)\ \pi_w(\tau_c - \tau_n + w)dw \end{aligned} \tag{17}$$

with $w_m \simeq 0$ a minimum waiting set by the finite size of the NW top facet.

Parameters b and B_T and function ϕ depend on the shape of the nucleus and also on its location *via* the edge energy γ_e, which is an average between portions of the nucleus edge in contact with the liquid and vapor phases.[4,12,24] For computational purposes, function ϕ can be expressed in terms of the Faddeeva (or Kramp) function $W(z) = \exp(-z^2)\mathrm{erfc}(-iz)$ or of its real and imaginary parts, the Voigt functions.

In Figure 4, we compare the distributions of all our characteristic times calculated numerically and analytically, using the same parameters (A, γ_e) in the corner nucleation rate (eqs 1 and 2) and the same arbitrary NW-droplet geometry ($R = 25$ nm, $\beta = 100°$). The simulation is carried out using the full expression of $\Delta\mu$ (see Supporting Information S1), including small size effects,[7] and taking into account desorption of As from the liquid. However, the temperature $T = 750$ K is set low enough to insure weak desorption, for sake of comparison with our analytical calculation. The remarkable agreement proves that approximation $\widehat{\Delta\mu}$ (eq 5) is excellent and that the few other simplifications made in our analytical calculation are amply justified. Our analytical calculation distributes quasi-perfectly the average ML cycle duration $\bar{\tau}_n = \bar{\tau}_c = N_{\mathrm{ML}}/\rho$ into the averages $\bar{w}$ and $\bar{p}$ and it also reproduces very well the widths and asymmetries of the distributions of the various characteristic times.

Analysis and modeling of the *in situ* experiments. In the NanoMAX equipment, we recorded, as described in Section Methods, long sequences of MLs on a single NW and at three *nominal* growth temperatures $T^{(n)} = 593$ K, 653 K and 713 K, termed low (subscript l), medium (m) and high (h) in the following. We took care to analyze sequences where the NW radius was stabilized at $R = 7$ nm and the contact angle at $\beta = 100°$. The experimental

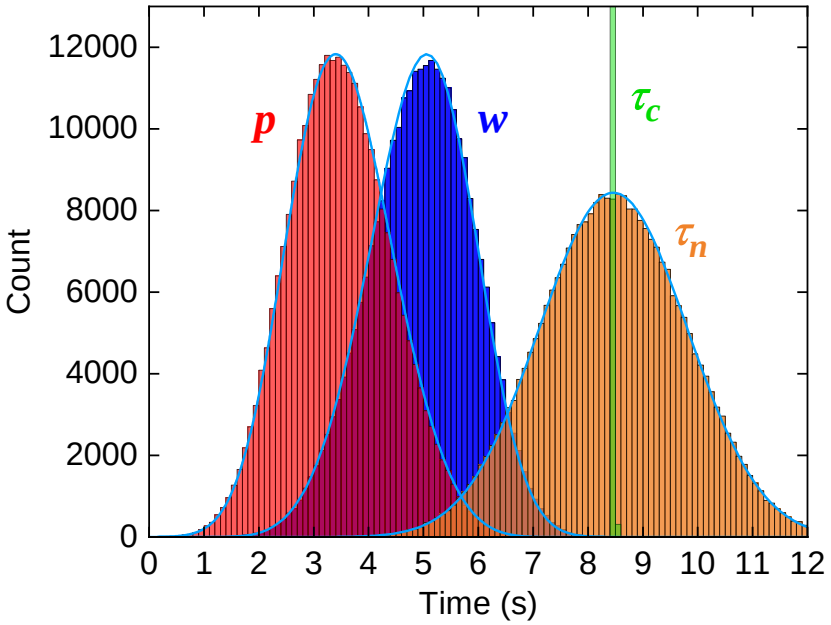

Figure 4: Histograms of the distributions of waiting times w, propagation times p and intervals τ_n between ML nucleations and τ_c between ML completions, obtained from numerical growth simulation at $T^{(c)} = 750$ K for a WZ NW with radius $R = 25$ nm and droplet contact angle $\beta = 100°$. Nucleation rate parameters are $A = 5.6857 \times 10^{24}$ m^{-2}s^{-1}, $\gamma_e = 0.2281$ J m^{-2}. The curves give the corresponding distributions calculated analytically using approximation $\widehat{\Delta\mu}$, with $\alpha_\mu = 1.00965$ and $x_{eq} = 2.7799 \times 10^{-4}$ (eq 5 and Supporting Information S1), scaled to the same total number of counts (except for τ_c).

histograms of times p, w, τ_n and τ_c were obtained as explained in Section Methods, taking into account the limited resolution due to the camera frame time $\delta = 0.25$ s. Histograms at the low and medium temperatures are shown in Figures 5 and 6 using unpatterned bars.

On the other hand, our numerical and analytical calculations yield the distributions of all characteristic times with arbitrary precision. Indeed, probability densities such as π_w or π_p (eqs 15 and 16) are continuous functions of their respective arguments and simulations can be carried out indefinitely. Therefore, in order to insure meaningful comparison between experiments and calculations, we smeared the computed results by mimicking the experimental detection process, as described in Section Methods.

We performed numerous growth simulations in order to reproduce our experiments. Apart from the geometrical parameters R and β, the only piece of information extracted from the experiments as input for modeling is the rate at which As is fed to the droplet.

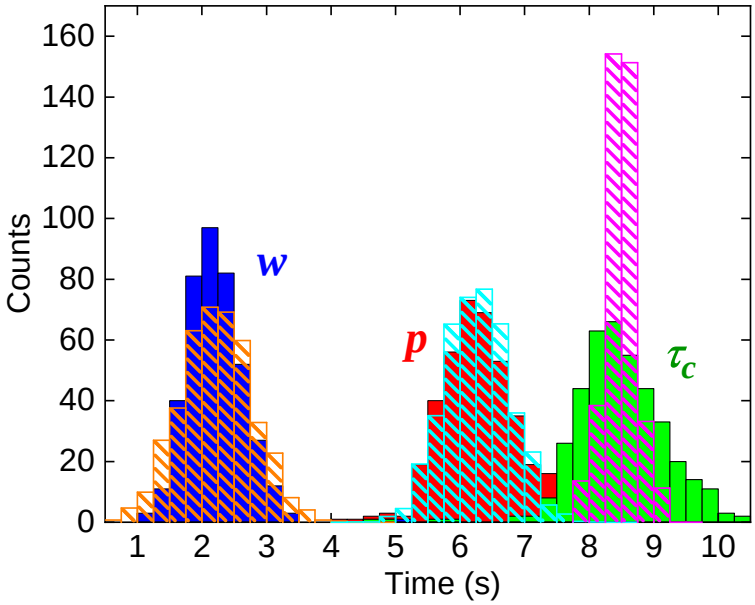

Figure 5: Histograms of waiting time w, propagation time p and time τ_c between ML completions measured at the low nominal temperature $T_l^{(n)} = 593$ K (full bars) and calculated at temperature $T_l^{(c)} = 770$ K using nucleation rate parameters $\ln A = 54.8$ (with A in $\mathrm{m^{-2}s^{-1}}$) and $\gamma_e = 0.20625$ J m^{-2} (hatched bars).

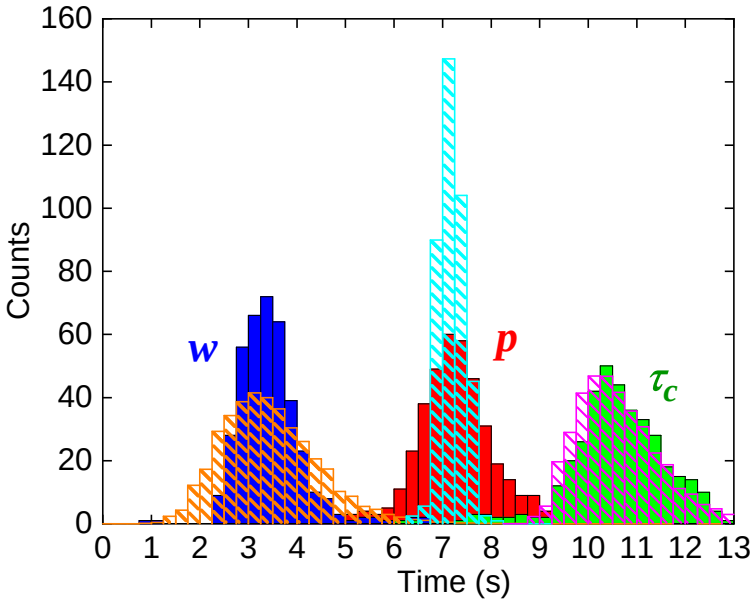

Figure 6: Same as Figure 5 for experiments at the medium nominal temperature $T_m^{(n)} = 653$ K (full bars) and calculations at temperature $T_m^{(c)} = 838$ K using nucleation rate parameters $\ln A = 59.5$ and $\gamma_e = 0.20625$ J m^{-2} (hatched bars).

Namely, ρ was chosen so as to produce the *average* value of the ML cycle duration ($\bar{\tau_c}$ or $\bar{\tau_n}$) measured at $T_l^{(n)} = 593$ K, a temperature at which As desorption from the liquid is very weak. The quantities that we varied between simulations are firstly the two nucleation rate parameters (eq 2), prefactor A and average step energy γ_e. These allow one to calculate the nucleation rate for any As concentration, since we know how $\Delta\mu$ depends on x and T (Supporting Information S1 and eq 5). The dependence of As desorption on x and T being also known,[7] we can then perform self-consistent growth simulations (and analytical calculations at low temperature).

It proved impossible to reproduce our three sets of experimental histograms by using the nominal temperatures $T^{(n)}$. We must set significantly higher calculation temperatures $T^{(c)}$ to get any agreement. This complicates the procedure a lot since the low, medium and high calculation temperatures $T_{l,m,n}^{(c)}$ add to A and γ_e as fit parameters. We now outline how we proceeded.

To quantify the discrepancy between experiments performed at nominal temperature $T^{(n)}$ on the one hand, and calculations carried out at temperature $T^{(c)}$ using nucleation rate parameters A and γ_e on the other, we consider the corresponding histograms of waiting and propagation times. We then define two distances between experiments and calculations, relative to the averages $\bar{w}$, $\bar{p}$ of the histograms and to their standard deviations σ_w, σ_p, respectively:

$$\begin{aligned} D_{av}\left(A,\gamma_e,T^{(c)},T^{(n)}\right) &= \left(\left[\bar{w}^{(c)}\left(A,\gamma_e,T^{(c)}\right)-\bar{w}^{(e)}\left(T^{(n)}\right)\right]^2\right. \\ &+ \left.\left[\bar{p}^{(c)}\left(A,\gamma_e,T^{(c)}\right)-\bar{p}^{(e)}\left(T^{(n)}\right)\right]^2\right)^{1/2} \qquad (18) \\ D_{sd}\left(A,\gamma_e,T^{(c)},T^{(n)}\right) &= \left(\left[\sigma_w^{(c)}\left(A,\gamma_e,T^{(c)}\right)-\sigma_w^{(e)}\left(T^{(n)}\right)\right]^2\right. \\ &+ \left.\left[\sigma_p^{(c)}\left(A,\gamma_e,T^{(c)}\right)-\sigma_p^{(e)}\left(T^{(n)}\right)\right]^2\right)^{1/2} \qquad (19) \end{aligned}$$

where superscripts (c) and (e) refer to calculations and experiments, respectively.

Figure 7 shows maps in plane $(\ln A, \gamma_e)$ of the coincidence between experiments carried

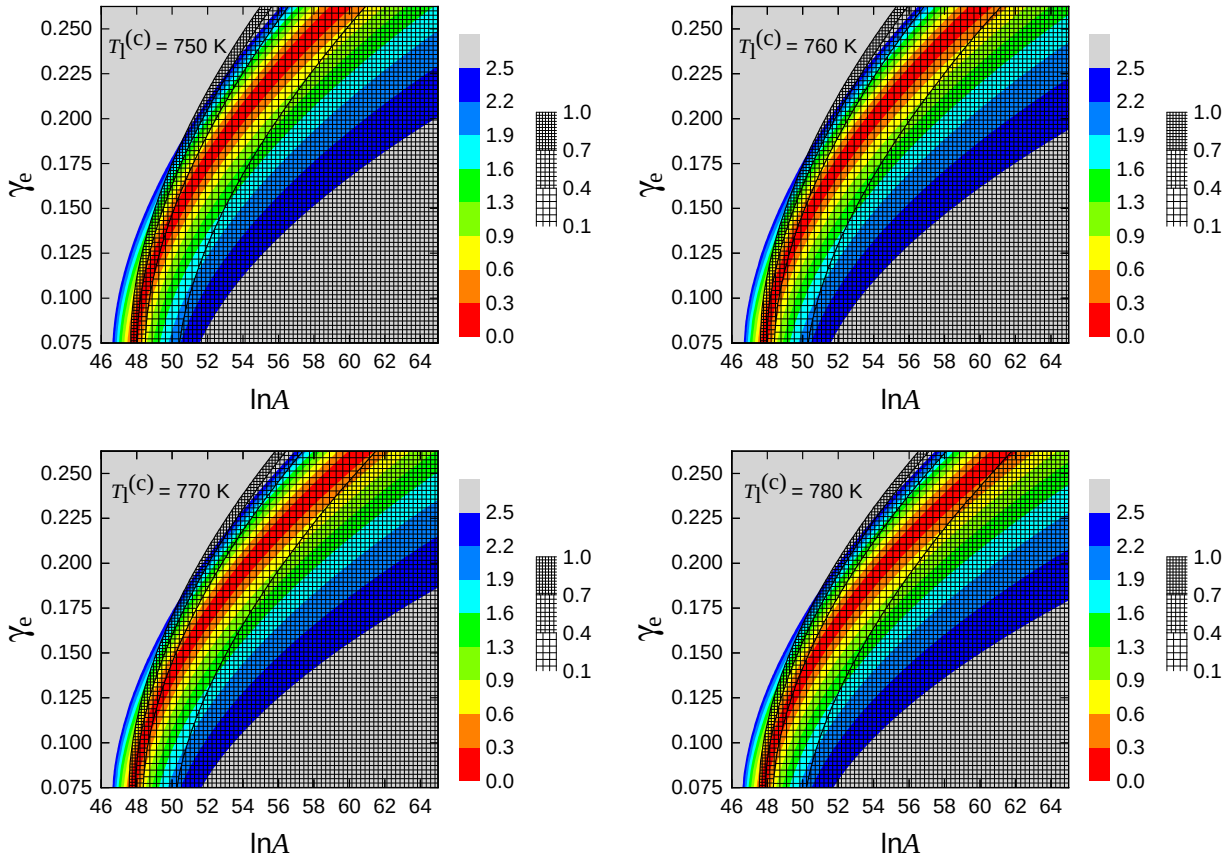

Figure 7: Discrepancy between experimental and calculated histograms of the propagation and waiting times, as a function of nucleation rate parameters A and γ_e used in the calculations. Experimental data were acquired at the low nominal growth temperature ($T_l^{(n)} = 593$ K) and calculations performed at the temperatures $T_l^{(c)}$ indicated in each panel. The discrepancy is quantified for both average values (D_{av}, eq 18, color-coded) and standard deviations (D_{sd}, eq 19, superimposed grid; for clarity, no grid is drawn for $D_{sd} > 1$).

out at $T_l^{(n)} = 593$ K and calculations at various temperatures $T_l^{(c)}$. Distance D_{av} is color-coded and distance D_{sd} is coded as a superimposed grid, with red color and loose grid corresponding to best agreement, respectively (the gridless zone corresponds to even worse fits of the standard deviations). Figure 8 shows similar maps for experiments at $T_m^{(n)} = 653$ K and another set of calculation temperatures $T_m^{(c)}$.

We first tried to reproduce all our experimental distributions using a single couple (A, γ_e), as suggested by our previous study of self-catalyzed ZB GaAs NWs, where we found that letting A change with T did not improve the match between experiments and calcu-

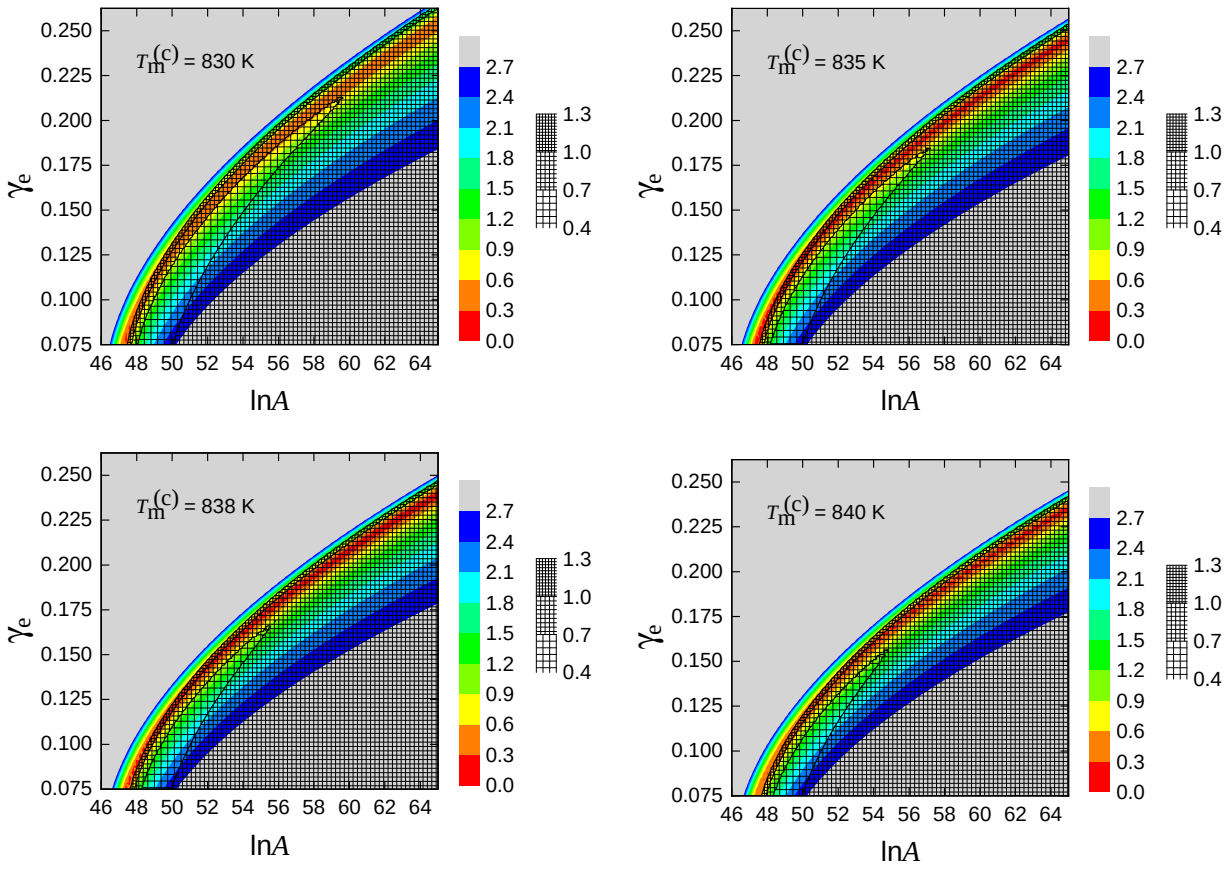

Figure 8: Same as Figure 7 for experiments performed at the medium nominal growth temperature ($T_m^{(n)} = 653$ K).

lations.[7] However, this work attempted only at reproducing the growth rate as a function of temperature and As flux, a task much less demanding than the present one. Moreover, A is actually expected to be temperature-dependent, since it incorporates several activated processes.[35] We therefore proceeded as follows.

For data acquired at nominal temperature $T_k^{(n)}$ $(k = l, m, h)$, we searched for a calculation temperature $T_k^{(c)}$ and parameters (A, γ_e) giving the best match. This proved critical for the medium temperature. A key point is that desorption should be large enough at $T_m^{(c)}$ to account for the significant increase of $\bar{w}^{(e)}$ observed between $T_l^{(n)}$ and $T_m^{(n)}$ (Figure 2). The maps of Figure 8 show that this narrowly constrains $T_m^{(c)}$ to around 830-840 K, well above $T_m^{(n)} = 653$ K. Only the maps with $T_m^{(c)}$ between 835 K and 838 K display D_{av} values below

0.3 s. For these temperatures, there is a whole band of parameters giving acceptable $\bar{p}$ and $\bar{w}$ values (low D_{av}) but it is not possible to achieve the best match with experiments simultaneously for averages and standard deviations. The distributions of Figure 6 (hatched histograms) were calculated at $T_m^{(c)} = 838$ K with $\ln A = 59.5$ (we take A in $\mathrm{m^{-2}s^{-1}}$) and $\gamma_e = 0.20625$ J m^{-2}. The average values of w, p and τ_c are all well reproduced by the calculations. Whereas the distributions of the waiting and propagation times are somewhat broader and narrower, respectively, than in the experiments, the τ_c distribution is particularly well modeled, including its marked asymmetry.

At the lowest nominal temperature $T_l^{(n)}$, where desorption is very weak, $T_l^{(c)}$ is not as severely constrained and a good match can be obtained simultaneously for averages and standard deviations (Figure 7). It is in particular possible to select a calculation temperature about 60 K below $T_m^{(c)}$, which preserves the nominal temperature difference. However, a good match cannot be realized for the $T_m^{(n)}$ and $T_l^{(n)}$ data using a single (A, γ_e) couple. The distributions of Figure 5 (hatched histograms) were calculated at $T_l^{(c)} = 770$ K with $\ln A = 54.8$ and the same $\gamma_e = 0.20625$ J m^{-2}, since we do not expect the edge energy to be very sensitive to temperature. Again, the partition of the ML cycle time between waiting and propagation times is very good and the standard deviations of these times are also well reproduced. The only discrepancy is that the calculated distribution of the ML cycle time τ_c is significantly narrower than the experimental one.

Finally, at the high nominal temperature, desorption is high, the growth rate much lower (Figure 2) and our data much noisier. Nevertheless, the steep increase of desorption with temperature obliges us to select a calculation temperature $T_h^{(c)}$ only 10 to 15 K above $T_m^{(c)}$.

The increase of A between $T_l^{(c)}$ and $T_m^{(c)}$ corresponds to an activation energy $E_a = 3.84$ eV. We simulated the evolution of the averages and standard deviations of the characteristic times with temperature, assuming $A(T)$ determined by E_a and a fixed $\gamma_e = 0.20625$ J m^{-2}. The results, shown in Figure 9, can be compared with the limited amount of experimental data of Figure 2. Our model reproduces correctly the moderate increase of the propagation time

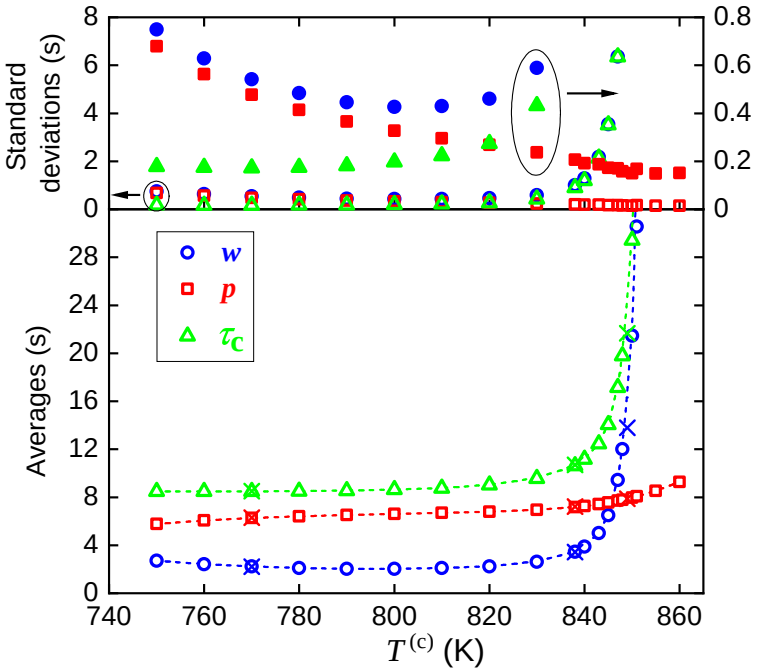

Figure 9: Evolution with growth temperature of the computed values of the averages and standard deviations of the characteristic times. In the lower panel, lines are visual guides and crosses repeat the experimental values of Figure 2 plotted at adjusted temperatures. In the upper panel, the same data are shown twice using identical open (left scale) and full (right scale) symbols.

with T and the much sharper increase of the waiting time, with the consequence that $\bar{w}$, and hence $\bar{\tau}_c$, become much larger than $\bar{p}$ at high temperature. This is due to desorption, given that x is larger during waiting time than during propagation (Figure 1b). As regards standard deviations, our calculations also reproduce correctly the sharp increase of σ_w with T. However, as explained earlier, they predict a decrease of σ_p. Although devoid of such a decrease, the experiments do indicate that σ_p increases only moderately, much more slowly than σ_w. Consequently, at high T, $\sigma_{\tau_c} \simeq \sigma_w$, as in our calculations.

Discussion. We have shown that our model can explain and reproduce most of the salient features of our experiments. There are however two discrepancies. First, we predict that, at high temperature, for most ML cycles, the liquid should reach a certain As concentration where desorption balances input, which has the effect of setting the following ML propagation time, since all fractional MLs formed at nucleation then have the same size

(Figure 3c). Very generally, given the frame rate δ and the data analysis discussed in Section Methods, fixed time intervals equal to $(n+\nu)\,\delta$, with n integer and $\nu < 1$, should produce a measured distribution with a standard deviation equal to $\sqrt{\nu\,(1-\nu)+1/4}\;\delta$. This value depends on temperature and incoming flux *via* ν and ranges between $\delta/2$ and $\delta/\sqrt{2}$. Our calculations predict a gradual decrease of the width of the p-distribution (Figure 9) and the values at high temperature are indeed in this range, which confirms that the dynamic balance between input and desorption is effectively realized. Experimentally, we do not observe such a decrease but rather a slight increase. As discussed below, statistical fluctuations might play a part in the larger measured standard deviations.

The second and most important difference is that our model predicts that, at low T (in the absence of desorption), time τ_c between ML completions should become very narrowly distributed even though, due to the stochasticity of nucleation, this is not the case for its components w and p. As mentioned above and explained in Section Methods, because of the detection delay and limited time resolution in NanoMAX (Figure 10), we do not expect to record the extremely narrow τ_c distributions calculated with a vanishing time resolution (Figure 4). Nevertheless, the low temperature experimental τ_c distribution appears broader than the distributions calculated with the appropriate finite time resolution (Figure 5).

These discrepancies between experiments and modeling might be related to extra statistical fluctuations. Since we are dealing with phases containing small numbers of As atoms, all numbers that we take as fixed or as evolving deterministically with time, might in fact fluctuate with respect to these values. This holds for the three phases considered, namely the input from vapor over a given time, the content of the liquid (in particular during ML propagation, when it is at its lowest) or the fractional ML. We have started to perform simulations taking some of these fluctuations into account. Although this broadens the τ_c distribution at low T and the p distribution at high T, we have not yet managed to reproduce the corresponding experimental values and further effort is necessary in this respect.

We showed that it was however possible to achieve quantitative agreement for a number

of measured quantities. This requires selecting calculation temperatures $T^{(c)}$ considerably higher than the nominal temperatures $T^{(n)}$ (Figures 5 to 8). The upward shift of the medium temperature is about 185 K. In this case, as already mentioned and demonstrated in Figure 8, temperature is narrowly constrained by the average ML cycle duration, which is very sensitive to desorption. As detailed in our previous work,[7] desorption is computed for any liquid As content x by using published formulas for the equilibrium pressures of the As molecules species, although admittedly these were themselves fitted on experimental data obtained at higher temperatures than ours. The choice of $T_l^{(c)}$ is much less critical: in the calculation, the average As concentration simply adjusts to provide a nucleation rate that matches the input rate. The nucleation rate depends on temperature (both directly and *via* $\Delta\mu$), but adjustment is possible over a wide range of temperature. As regards $T_h^{(c)}$, we must choose it fairly close to $T_m^{(c)}$ (Figure 9), but the difference with $T_h^{(n)}$ is still larger than 100 K. As a possible explanation for these shifts, we note that growth is performed on Joule-heated membranes and $T^{(n)}$ given by a current-temperature calibration performed by the manufacturer. However, deposition of material on the membrane during NW growth and possible extra heating by the electron beam may alter this relationship.

As discussed above, agreement between measurements and calculations also requires a careful selection of the nucleation rate parameters A and γ_e. The values that we used at $T_l^{(c)}$ and $T_m^{(c)}$ are however not unique (see Figures 7 and 8). We made the reasonable choice of assuming a temperature-independent edge energy γ_e (and a single activation energy for prefactor A to extend our calculations at other temperatures), but this is not warranted. Recalling that, for corner nucleation of rhomboidal nuclei, γ_e is the mean of the energies γ_1 and $\gamma_0 \simeq \gamma_1/4$ of the nucleus edge segments in contact with liquid and vapor,[12] the value quoted above corresponds to $\gamma_1 = 0.31$ J m^{-2}, significantly more than what we determined in our previous study of self-catalyzed ZB GaAs NWs (0.123 J m^{-2}).[7]

Probably the most spectacular prediction of our model is that, provided growth is performed at low temperature, the time τ_c between the completion of successive MLs should be

fixed, despite the random occurrence of the nucleation events. This implies that the length of a NW section could be set without error simply by selecting the appropriate growth time, to which it would be proportional, at a given group V flux. This might enable the fabrication of axial heterostructures with precisely controlled dimensions, such as quantum disks or quantum dots, in a standard growth setup devoid of real time *in situ* monitoring. Control of such structures at the ML level is actually necessary for promising applications.[41–43] Note that in case group V sidewall diffusion would also contribute to droplet refill (which we recently found likely for P species[33]), this would only require stems longer than the corresponding short diffusion length, in addition to constant NW and droplet radii.[34,44] We showed that the reason for this quasi-deterministic growth regime is the compensation between the propagation time and preceding waiting time, expected to occur when there is never enough group V atoms in the catalyst particle to produce a full ML at nucleation. Such *complementarity* between times w and p appears as the opposite of the situation recently studied by Maliakkal *et al.*,[13] who showed that, on the contrary, in the case of Au-catalyzed GaAs NWs, it is possible to control *independently* w and p through the group III and group V fluxes, respectively. In view of the applications just mentioned, we believe that the precise control of an intrinsically uniform ML cycle time is even more promising. On the experimental side, the next steps will thus be to record growth sequences using a faster camera (although this could reduce the signal to noise ratio and thwart the precise detection of ML nucleation and completion) and to track down possible residual instabilities of our growth conditions. In parallel, we will attempt to understand if some growth mechanism or intrinsic fluctuations so far neglected might hinder the achievement of the quasi-deterministic growth regime.

METHODS

***In situ* transmission electron microscopy.** We observed the growth of GaAs NWs *in situ* using the NanoMAX equipment, a Cs-corrected Titan TEM equipped with custom-

made MBE sources. These sources are highly collimated so that the evaporated material only deposits onto the sample. The substrate was a Protochips heating SiC membrane with holes of 10 µm diameter. Pure Ga and As were loaded into boron nitride crucibles and heated to about 930 and 320°C, respectively. A needle valve allowed us to adjust the As flux to the precise value ensuring stable growth conditions over a long period of time. The As flux was monitored using a cold cathode gauge mounted in the proximity of the connection between the As source and the microscope column. This minimized the change in droplet size and NW diameter, which could lead to a drift in the average growth rate. The average growth rate varied between 0.12 and 0.04 ML per second, depending on the substrate temperature. These low growth rates were selected to allow us to record enough frames during each ML cycle, thereby minimizing the error on the time measurements. Ga was initially deposited on the substrate at a nominal temperature of 500°C and when the Ga droplets reached the size of 20-30 nm, As was introduced and the temperature decreased to a nominal temperature of 420°C to promote the growth of NWs. The substrate temperature was then modified during the different phases of the experiment. Due to the polycrystalline nature of the SiC substrate, NWs started growing in arbitrary directions on the substrate or freely suspended in vacuum across the holes. The sample was then tilted to orientate the selected NW a few degrees off the <110> zone axis, in order to observe an areal projection of the NW-droplet interface. We argued previously that this is necessary to determine accurately the nucleation and completion times of each ML, whereas observations made with the interface parallel to the electron beam may be misleading.[12] All data were collected on the same NW. High-resolution movies were recorded using a Gatan US1000 camera at a rate of 4 frames per second. Images were analyzed manually.

Experimental histograms from *in situ* measurements and their computation. The NanoMAX camera acquires images at fixed times $t_i = i\delta$ (i integer), with $1/\delta$ the frame rate. Any of our characteristic times (w, p $\cdots$) is actually the interval between a start time t_s and a finish time t_f, but the corresponding events are only detected after they

happen, hence (at best) at t_j, t_k, with $t_{j-1} < t_s \leq t_j$, $t_{k-1} < t_f \leq t_k$. For each ML No i in a given growth sequence, we measured time $t_n(i)$ at which nucleation and fast initial propagation are observed (stage 1) and time $t_c(i)$, marking ML completion at end of stage 2. For this ML, the *apparent* propagation time is $p = t_c(i) - t_n(i)$, the following waiting time is $w = t_n(i+1) - t_c(i)$, and the ML cycle times are, for instance, $\tau_n = t_n(i+1) - t_n(i)$ and $\tau_c = t_c(i) - t_c(i-1)$. The same apparent characteristic time $t_k - t_j = (k-j)\delta$ is thus attributed to pairs of events that can actually be separated by intervals ranging between just above $(k-j-1)\delta$ (*e.g.* red disks in figure 10, top) and just below $(k-j+1)\delta$ (*e.g.* blue triangles in figure 10, top). This leads us to define experimental histograms with bins of width δ, bin No n being $[n\delta, (n+1)\delta]$, and then, for each recorded duration $(k-j)\delta$, to attribute 0.5 count to both bins Nos $k-j-1$ and $k-j$ (figure 10, bottom). It would not make sense to define bins of width 2δ, since the events marked by green squares in the figure will also contribute 0.5 count to bin No $k-j$ but none to bin $k-j-1$.

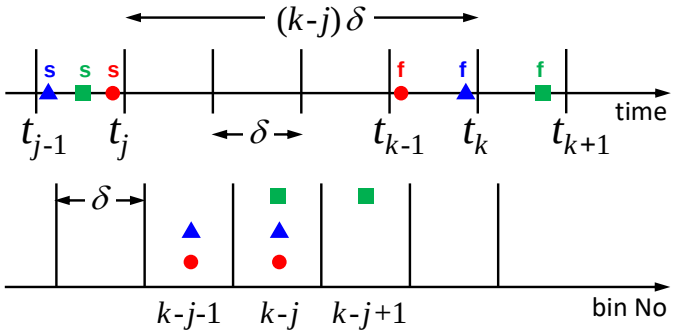

Figure 10: Top: Each symbol type marks the possible start (s) and finish (f) of a certain characteristic time. Red disk and blue triangle starts are both detected at t_j and the corresponding finishes at t_k, although the first characteristic time lasts only slightly more than $t_{k-1} - t_j = (k-j-1)\delta$ and the second one slightly less than $t_k - t_{j-1} = (k-j+1)\delta$. Bottom: Schematics of the neighboring pairs of histogram bins to which each characteristic time in the top diagram is affected. Here, each symbol counts for 0.5.

On the other hand, our numerical and analytical calculations yield the distributions of all characteristic times with arbitrary precision. Nevertheless, to insure proper comparison between experiments and calculations, we also computed NanoMAX-type histograms with the same bins of width δ as follows. In the simulations of the growth sequences, we simply

mimicked the experimental process by considering that each event (nucleation or completion of a ML), although precisely dated, is detected at the next multiple of δ. As for the analytical calculations, they yield continuous probability distributions π_τ of any characteristic time τ (eqs 15-17). A characteristic time $\tau = (n + \epsilon)\,\delta$ (n integer, $\epsilon < 1$) starts equiprobably within any time interval of width δ. Its beginning and end will thus be detected with probability $(1 - \epsilon)$ at times separated by $n\delta$ (this contribution should thus be shared equally between bins Nos $(n - 1)$ and n) and with probability ϵ at times separated by $(n + 1)\delta$ (to be shared equally between bins Nos n and $(n + 1)$). Finally, the contribution to bin No n will be proportional to:

$$I_n = \int_{(n-1)\delta}^{n\delta} \left(\frac{\tau}{\delta} - n + 1\right) \pi_\tau(\tau)d\tau + \int_{n\delta}^{(n+1)\delta} \pi_\tau(\tau)d\tau + \int_{(n+1)\delta}^{(n+2)\delta} \left(n + 2 - \frac{\tau}{\delta}\right) \pi_\tau(\tau)d\tau \quad (20)$$

Acknowledgement

We thank Agence Nationale de la Recherche for funding the NanoMAX equipment, within "Equipements d'excellence" Project No 10-EQPX-0050 TEMPOS (Transmission Electron Microscopy at Palaiseau-Orsay-Saclay) and CIMEX at École polytechnique (Palaiseau) where this equipment is hosted. We also thank E. Leshchenko (Lunds University) for contributing to the analysis of the experimental data during a secondment period at C2N, within the European Union Marie Skłodowska-Curie INDEED project (grant agreement No 722176).

Supporting Information Available

S1: Difference of chemical potential between a (Ga,As) liquid and solid GaAs (pdf)

Movie1. Nucleation and propagation of 5 MLs during the growth of a WZ GaAs NW. Ga and As crucibles were set at about 930 and 320 °C, respectively, and As pressure to 1.07×10^{-5} Torr. The movie, recorded at a frame rate of 4 fps, is played at 12 fps. The graph shows the fraction θ of the NW-liquid interface covered successively by each ML. (avi)

References

1. Dubrovskii, V. G.; Sibirev, N. V.; Cirlin, G. E.; Harmand, J. C.; Ustinov, V. M. Theoretical analysis of the vapor-liquid-solid mechanism of nanowire growth during molecular beam epitaxy. *Phys. Rev. E* **2006**, *73*, 021603.

2. Kashchiev, D. Dependence of the growth rate of nanowires on the nanowire diameter. *Cryst. Growth Des.* **2006**, *6*, 1154–1156.

3. Johansson, J.; Karlsson, L. S.; Svensson, C. P. T.; Mårtensson, T.; Wacaser, B. A.; Deppert, K.; Samuelson, L.; Seifert, W. Structural properties of <111>B-oriented III-V nanowires. *Nat. Mater.* **2006**, *5*, 574–580.

4. Glas, F.; Harmand, J. C.; Patriarche, G. Why does wurtzite form in nanowires of III-V zinc blende semiconductors? *Phys. Rev. Lett.* **2007**, *99*, 146101.

5. Wen, C.-Y.; Tersoff, J.; Hillerich, K.; Reuter, M. C.; Park, J. H.; Kodambaka, S.; Stach, E. A.; Ross, F. M. Periodically changing morphology of the growth interface in Si, Ge, and GaP nanowires. *Phys. Rev. Lett.* **2011**, *107*, 025503.

6. Krogstrup, P.; Curiotto, S.; Johnson, E.; Aagesen, M.; Nygård, J.; Chatain, D. Impact of the liquid phase shape on the structure of III-V nanowires. *Phys. Rev. Lett.* **2011**, *106*, 125505.

7. Glas, F.; Ramdani, M. R.; Patriarche, G.; Harmand, J.-C. Predictive modeling of self-catalyzed III-V nanowire growth. *Phys. Rev. B* **2013**, *88*, 195304.

8. Krogstrup, P.; Jørgensen, H. I.; Johnson, E.; Madsen, M. H.; Sørensen, C. B.; Fontcuberta i Morral, A.; Aagesen, M.; Nygård, J.; Glas, F. Advances in the theory of III-V nanowire growth dynamics. *J. Phys. D: Appl. Phys.* **2013**, *46*, 313001.

9. Dubrovskii, V. G.; Glas, F. In *Fundamental properties of semiconductor nanowires*; Fukata, N., Rurali, R., Eds.; Springer: Singapore, 2021; pp 3–107.

10. Gamalski, A. D.; Ducati, C.; Hofmann, S. Cyclic supersaturation and triple phase boundary dynamics in Germanium nanowire growth. *J. Phys. Chem. C* **2011**, *115*, 4413–4417.

11. Jacobsson, D.; Panciera, F.; Tersoff, J.; Reuter, M. C.; Lehmann, S.; Hofmann, S.; Dick, K. A.; Ross, F. M. Interface dynamics and crystal phase switching in GaAs nanowires. *Nature* **2016**, *531*, 317–322.

12. Harmand, J.-C.; Patriarche, G.; Glas, F.; Panciera, F.; Florea, I.; Maurice, J.-L.; Travers, L.; Ollivier, Y. Atomic step flow on a nanofacet. *Phys. Rev. Lett.* **2018**, *121*, 166101.

13. Maliakkal, C. B.; Mårtensson, E. K.; Tornberg, M. U.; Jacobsson, D.; Persson, A. R.; Johansson, J.; Wallenberg, L. R.; Dick, K. A. Independent control of nucleation and layer growth in nanowires. *ACS Nano* **2020**, *14*, 3868–3875.

14. Panciera, F.; Baraissov, Z.; Patriarche, G.; Dubrovskii, V. G.; Glas, F.; Travers, L.; Mirsaidov, U.; Harmand, J.-C. Phase selection in self-catalysed GaAs nanowires. *Nano Lett.* **2020**, *20*, 1669–1675.

15. Glas, F. Chemical potentials for Au-assisted vapor-liquid-solid growth of III-V nanowires. *J. Appl. Phys.* **2010**, *108*, 073506.

16. Glas, F.; Harmand, J. C.; Patriarche, G. Nucleation antibunching in catalyst-assisted nanowire growth. *Phys. Rev. Lett.* **2010**, *104*, 135501.

17. Glas, F. Statistics of sub-Poissonian nucleation in a nanophase. *Phys. Rev. B* **2014**, *90*, 125406.

18. Glas, F.; Dubrovskii, V. G. Self-narrowing of size distributions of nanostructures by nucleation antibunching. *Phys. Rev. Mater.* **2017**, *1*, 036003.

19. Koivusalo, E. S.; Hakkarainen, T. V.; Guina, M. D.; Dubrovskii, V. G. Sub-Poissonian

narrowing of length distributions realized in Ga-catalyzed GaAs nanowires. *Nano Lett.* **2017**, *17*, 5350–5355.

20. Tauchnitz, T.; Berdnikov, Y.; Dubrovskii, V. G.; Schneider, H.; Helm, M.; Dimakis, E. A simple route to synchronized nucleation of self-catalyzed GaAs nanowires on silicon for sub-Poissonian length distributions. *Nanotechnology* **2018**, *29*, 504004.

21. Oh, S. H.; Chisholm, M. F.; Kauffmann, Y.; Kaplan, W. D.; Luo, W.; Rühle, M.; Scheu, C. Oscillatory mass transport in vapor-liquid-solid growth of sapphire nanowires. *Science* **2010**, *330*, 489.

22. Gil, E.; Dubrovskii, V. G.; Avit, G.; André, Y.; Leroux, C.; Lekhal, K.; Grecenkov, J.; Trassoudaine, A.; Castelluci, D.; Monier, G.; Ramdani, R. M.; Robert-Goumet, C.; Bideux, L.; Harmand, J. C.; Glas, F. Record pure zincblende phase in GaAs nanowires down to 5 nm in radius. *Nano Lett.* **2014**, *14*, 3938–3944.

23. Dubrovskii, V. G. Refinement of nucleation theory for vapor-liquid-solid nanowires. *Cryst. Growth Des.* **2017**, *17*, 2589–2593.

24. Glas, F.; Dubrovskii, V. G. Energetics and kinetics of monolayer formation in vapor-liquid-solid nanowire growth. *Phys. Rev. Mater.* **2020**, *4*, 083401.

25. Rusanov, A. I. The thermodynamics of processes of new-phase formation. *Russian Chem. Rev.* **1964**, *33*, 385–399.

26. Rao, M.; Berne, B. J. Nucleation in finite systems: theory and computer simulation. *Astrophys. Space Sci.* **1979**, *65*, 39–46.

27. Schmelzer, J. W. P.; Abyzov, A. S. Thermodynamic analysis of nucleation in confined space: Generalized Gibbs approach. *J. Chem. Phys.* **2011**, *134*, 054511.

28. Wilhelmsen, Ø.; Bedeaux, D.; Kjelstrup, S.; Reguera, D. Superstabilization of fluids in nanocontainers. *J. Chem. Phys.* **2014**, *141*, 071103.

29. Wen, C.-Y.; Tersoff, J.; Reuter, M. C.; Stach, E. A.; Ross, F. M. Step-flow kinetics in nanowire growth. *Phys. Rev. Lett.* **2010**, *105*, 195502.

30. Dubrovskii, V. G.; Sibirev, N. V.; Harmand, J. C.; Glas, F. Growth kinetics and crystal structure of semiconductor nanowires. *Phys. Rev. B* **2008**, *78*, 235301.

31. Ramdani, M. R.; Harmand, J. C.; Glas, F.; Patriarche, G.; Travers, L. Arsenic pathways in self-catalyzed growth of GaAs nanowires. *Cryst. Growth Des.* **2013**, *13*, 91–96.

32. Oehler, F.; Cattoni, A.; Scaccabarozzi, A.; Patriarche, G.; Glas, F.; Harmand, J.-C. Measuring and modelling the growth dynamics of self-catalyzed GaP nanowire arrays grown by MBE. *Nano Lett.* **2018**, *18*, 701–708.

33. Pishchagin, A.; Glas, F.; Patriarche, G.; Cattoni, A.; Harmand, J.-C.; Oehler, F. Dynamics of droplet consumption in vapor-liquid-solid III-V nanowire growth. *Cryst. Growth Des.* **2021**, *21*, 4647–4655.

34. Dubrovskii, V. G.; Cirlin, G. E.; Soshnikov, I. P.; Tonkikh, A. A.; Sibirev, N. V.; Samsonenko, Y. B.; Ustinov, V. M. Diffusion-induced growth of GaAs nanowhiskers during molecular beam epitaxy: Theory and experiment. *Phys. Rev. B* **2005**, *71*, 205325.

35. Markov, I. N. *Crystal growth for beginners*; World Scientific: Singapore, 2003.

36. Venables, J. A.; Spiller, G. D. T.; Hanbucken, M. Nucleation and growth of thin films. *Rep. Prog. Phys.* **1984**, *47*, 399–459.

37. Kashchiev, D. *Nucleation*; Elsevier: Oxford, 2000.

38. Sobanska, M.; Dubrovskii, V. G.; Tchutchulashvili, G.; Klosek, K.; Zytkiewicz, Z. R. Analysis of incubation times for the self-induced formation of GaN nanowires: Influence of the substrate on the nucleation mechanism. *Cryst. Growth Des.* **2016**, *16*, 7205–7211.

39. Barbier, C.; Zhou, T.; Renaud, G.; Glas, F.; Geaymond, O.; Madouri, A.; Cavanna, A.; Travers, L.; Morassi, M.; Gogneau, N.; Tchernycheva, M.; Harmand, J.-C.; Largeau, L.

In situ X-ray diffraction study of GaN nucleation on transferred graphene. *Cryst. Growth Des.* **2020**, *20*, 4013–4019.

40. Abramowitz, M.; Stegun, I. A. *Handbook of mathematical functions*; Dover: New York, 1970.

41. Bouwes Bavinck, M.; Jöns, K. D.; Zieliński, M.; Patriarche, G.; Harmand, J.-C.; Akopian, N.; Zwiller, V. Photon cascade from a single crystal phase nanowire quantum dot. *Nano Lett.* **2016**, *16*, 1081–1085.

42. Taherkhani, M.; Willatzen, M.; Denning, E. V.; Protsenko, I. E.; Gregersen, N. High-fidelity optical quantum gates based on type-II double quantum dots in a nanowire. *Phys. Rev. B* **2019**, *99*, 165305.

43. Hastrup, J.; Leandro, L.; Akopian, N. All-optical charging and charge transport in quantum dots. *Sci. Rep.* **2020**, *10*, 14911.

44. Ruth, V.; Hirth, J. P. Kinetics of diffusion-controlled whisker growth. *J. Chem. Phys.* **1964**, *41*, 3139–3149.